





# Intrinsic spin-dynamical properties of two-dimensional half-metallic FeX<sub>2</sub> (X = Cl, Br, I) ferromagnets: Insight from density functional theory calculations

Ram Krishna Ghosh <sup>\*</sup>, Ashna Jose , and Geetu Kumari 

*Special Centre for Nanoscience, Jawaharlal Nehru University, New Delhi-110067, India*

 (Received 26 August 2020; revised 8 December 2020; accepted 27 January 2021; published 4 February 2021)

Ultrathin two-dimensional (2D) ferromagnets with intrinsic half-metallicity are highly prospective in designing nanoscale spintronics devices. In this work, we systematically investigate the spin transport and dynamical properties of one such group of promising 2D ferromagnets—monolayer iron dihalides (FeX<sub>2</sub>, X = Cl, Br, I)—using density functional theory (DFT). First, we explore the spin transport properties of these FeX<sub>2</sub> monolayers by combining the nonequilibrium Green's function (NEGF) technique with DFT. This study shows an inherent half-metallicity with a large spin gap that offers 100% spin-polarization over a wide Fermi window (>1 eV). We then focus on understanding their magnetocrystalline anisotropy, Gilbert damping, and exchange interactions, in-depth, which are the key aspects in controlling the spin dynamics. We use force theorem to determine the magnetocrystalline anisotropy and Kambersky's torque-torque correlation model for Gilbert damping. Our calculations reveal a sizable perpendicular anisotropy (0.04 to 0.25 mJ/m<sup>2</sup>) along with a relatively low Gilbert damping ( $7.9 \times 10^{-5}$  to  $3.7 \times 10^{-4}$ ) in these materials. Using spin-polarized Green's function formalism, we finally explore the effective exchange interactions in these materials and determine their spin-wave stiffness, exchange stiffness constants, and Curie temperatures. All these calculations, collectively, provide significance of these 2D FeX<sub>2</sub> ferromagnets for next-generation spintronics applications.

DOI: [10.1103/PhysRevB.103.054409](https://doi.org/10.1103/PhysRevB.103.054409)

## I. INTRODUCTION

Half-metallic ferromagnets (HMFs), having complete spin-polarization at the Fermi level ( $\epsilon_f$ ), are one of the most efficient spin source materials for magnetic tunnel junctions (MTJs) or spin-valve devices [1,2]. Particularly, the ability to generate pure spin current, large magnetoresistance, higher spin injection efficiency, and lowering the power consumption make them very promising in developing high-performance magnetic memory and logic devices [1–6]. Due to these facts, several HMFs have been identified, to date, although most of them are in their three-dimensional (3D) bulk form. For instance, different Heusler alloys, transition metal oxides/chalcogenides, and double perovskites have been found as promising 3D HMF-materials and are explored successfully in various spintronics devices [6–9]. However, maintaining a long-range magnetic ordering is quite difficult while lowering the dimensions of these systems for nanoscale device fabrication [10]. In that sense, magnetic 2D van der Waals (vdW) materials are of good choice due to their inherent broken spin rotational symmetry that allows them to maintain a magnetic ground state even in the single-layer limit [11]. Recently, various experimental studies also confirm the existence of sufficient ferromagnetism in monolayers of different magnetic vdW materials, (e.g., CrI<sub>3</sub>, VSe<sub>2</sub>, MnSe<sub>2</sub>, etc.) [11–14], and this indeed opens a new era of designing spintronics devices at the nanoscale regime [15]. However, if we see this class of materials, most of them do not possess intrinsic

half-metallicity. Thus, several alternative approaches are adopted, like surface adsorption, doping, edge modification, interface engineering, or even defect engineering to introduce half-metallicity in them [16,17]. Unfortunately, all these methods add more complexity in synthesizing these vdW materials. To overcome this, currently, 2D vdWs with intrinsic half-metallicity have gained significant attention in designing ultrathin spintronics devices. In this aspect, the family of FeX<sub>2</sub> monolayers has recently emerged as promising candidates due to their robust intrinsic half-metallic properties. This system basically came to light when Torun *et al.* [18] theoretically predicted a high magnetic moment ( $4 \mu_B$ /unit cell) and exceptionally large spin gap ( $\sim 4.5$  eV) for FeCl<sub>2</sub> monolayer. In fact, this wide spin gap is highly suited in reducing spin-flipping or spin-leakage in nanoscale devices [3,19]. Since then, many theoretical investigations on FeX<sub>2</sub> monolayers were carried out which were mainly devoted to their structural properties and half-metallicity [19–21]. Recently, Ashton *et al.* [19], along with these basic investigations, have further extended their theoretical analysis to magnetocrystalline anisotropy energy to determine the ferromagnetic ordering of these materials.

However, half-metallicity, solely, is not a deterministic factor for practical applications of any material for spin-based device fabrication. To assess the potential of the material for realistic applications, it is also necessary to understand its spin-dynamical properties, which are governed by the Landau-Lifshitz-Gilbert (LLG) equation [22],

$$\frac{\partial \mathbf{m}}{\partial t} = -\gamma(\mathbf{m} \times \mathbf{H}_{\text{eff}}) + \alpha \left( \mathbf{m} \times \frac{\partial \mathbf{m}}{\partial t} \right), \quad (1)$$

<sup>\*</sup>ramki.phys@gmail.com

where,  $m(=M/M_s)$  is the normalized magnetic spin moment (with  $M_s$  as the saturation magnetization),  $\gamma$  is the gyromagnetic ratio, and  $\alpha$  is the Gilbert damping parameter. Within the effective magnetic field  $\mathbf{H}_{\text{eff}} (= -\partial E[\mathbf{M}]/\partial \mathbf{M})$  in Eq. (1), the free-energy functional  $E[\mathbf{M}]$  has three main contributions; magnetocrystalline anisotropy (MCA), exchange interaction (EXC), and external field energy [23]. This MCA, originating from the spin-orbit interactions (SOC) of a material, is a key parameter that decides the energetically favorable magnetization direction of a crystal (called as easy axis) and plays a crucial role in determining the thermal stability of spin-transfer-torque based magnetic random access memories (STT-MRAMs) [24,25]. Similarly, EXC is also a material property that controls the alignment of neighboring moments and describes different dynamical phenomena, like magnetic vortices, skyrmions, etc., in ferromagnets [26]. Moreover, this EXC along with the MCA determines the magnetic domain wall-width and exchange-length in STT-MRAMs [27]. Besides, the Gilbert damping, which regulates the magnetization precession in Eq. (1), also helps in realizing the spin pumping phenomena (that generates pure spin current by magnetization dynamics) as well as the response speed of STT-MRAMs [24,25,28]. Therefore, understanding and quantification of these intrinsic magnetic properties are highly necessary to determine the performances of spintronics devices based on these materials. However, to the best of our knowledge, there is no systematic study yet to determine all these intrinsic spin-dynamical properties of  $\text{FeX}_2$  monolayers, which is the scope of this work.

With this aim, we present here the spin transport and dynamical properties of these  $\text{FeX}_2$  monolayers by means of DFT. At first, we provide a general overview of the crystallographic nature and stability of these crystals prior to investigating the spin-dependent transport properties using spin-polarized DFT and NEGF. The detailed analysis reveals not only a robust half-metallicity of these materials as reported in the literature [18–21] but also a high conductance over a wide Fermi window. We then evaluate the MCA energy at the atomic level using the “force theorem” and adopt Kambersky’s torque-torque correlation model to determine the Gilbert damping tensors. Finally, we estimate the effective exchange-coupling constants, employing spin-polarized Green’s function formalism, and analyze the spin-wave stiffness, exchange stiffness constants and Curie temperatures of this group of materials. This spin-dynamical analysis for the 2D vdW materials, especially at the atomic level, is rarely found in the literature and, thus, will be pioneering for 2D-spintronics applications.

## II. COMPUTATIONAL DETAILS

The calculations of different electronic and magnetic properties of monolayer  $\text{FeX}_2$  were performed using DFT, as implemented in QuantumATK [29]. Within the generalized gradient approximation (GGA), a Perdew-Burke-Ernzerhof (PBE) functional with SG15 type of norm-conserving Vanderbilt pseudopotentials (PPs) and high basis set were used to describe the exchange-correlation effects [30]. In addition, a well converged  $\Gamma$ -centered  $k$ -point sampling of  $(21 \times 21 \times 1)$  and cutoff energy of 160 Ryd were used for these calculations,

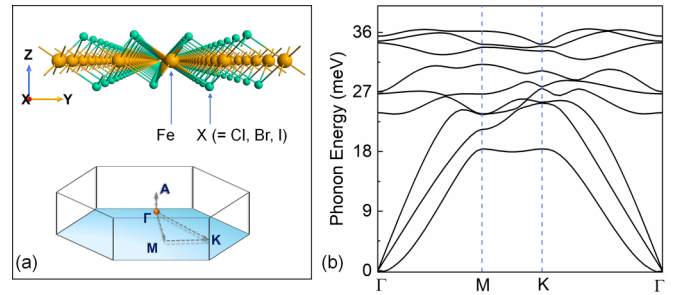


FIG. 1. (a) Side view of monolayer 1T  $\text{FeX}_2$  crystals and their corresponding first Brillouin zone. (b)  $\text{FeCl}_2$  phonon band structure, a representative phonon dispersion of monolayer 1T  $\text{FeX}_2$ .

unless specified. Besides, for controlling the iterations, Pulay mixer algorithm was used along with a tolerance of  $10^{-5}$  between two consecutive steps. The primitive unit cell of monolayer  $\text{FeX}_2$  contains one functional unit (f.u.), i.e., one Fe and two X ( $X = \text{Cl, Br, I}$ ) atoms. Moreover, to make a monolayer, a thick vacuum of 20 Å along the  $c$  axis (while retaining the lattice parameters “ $a$ ” and “ $b$ ” as periodic) was used to minimize the interactions between the periodic images of the layers. The optimized crystallographic structures were obtained by Broyden-Fletcher-Goldfarb-Shannon (LBFGS) scheme until the residual forces acting on atoms were mitigated to less than  $0.005 \text{ eV}/\text{Å}$  and the stress was less than  $0.0001 \text{ eV}/\text{Å}^3$ , to reach the minimum-energy configurations. Alongside this, a frozen phonon method with a  $9 \times 9 \times 1$  supercell was employed to obtain phonon dispersions to illustrate the structural stability of all these  $\text{FeX}_2$  crystals. To note, the calculated results of different structural, electronic and magnetic properties using SG15 PPs are also consistent with the results obtained by plane-wave PPs in QuantumATK. Besides, the main technicalities and necessary theories of different calculations are included in individual sections.

## III. RESULTS AND DISCUSSION

### A. Crystal structure and stability

Iron dihalides are inherently layered structures and, in their bulk form, can adopt two different polymorphs, namely trigonal (space group:  $P\bar{3}m1$ ) or rhombohedral (space group:  $R\bar{3}m$ ), depending on the geometrical orientation of stacked layers [31]. As often seen, the individual layer has octahedrally coordinated  $[\text{FeX}_6]^{4-}$  units, forming a triangular arrangement of X-Fe-X atoms in each of the  $\text{FeX}_2$  layers [see Fig. 1(a)]. Whereas, each layer stacks along the  $c$  axis in two different ways by weak vdW force to produce trigonal and rhombohedral bulk form. Therefore, we can say that the  $\text{FeX}_2$  monolayers, extracted from different bulk polymorphs are of similar structure (usually called as a 1T phase) and belong to a  $C_{3v}$  point group symmetry [18–20]. Our calculations show that this 1T configuration of  $\text{FeX}_2$  monolayers is the most stable configuration, and has much lower formation energy (defined as,  $E_{\text{form}} = E_{\text{FeX}_2} - E_{\text{Fe}} - 2E_{\text{X}}$ ) than the other possible form, hexagonal 1H, which is frequently found as a stable state in transition metal dichalcogenides [32]. For instance, the energy of 1T form of  $\text{FeCl}_2$  monolayer is lower by  $\sim 0.26 \text{ eV}/\text{unit cell}$  than its 1H form (see Supplemental Material

TABLE I. Lattice parameter ( $a$ ), average Fe-X-Fe angle ( $\vartheta$ ), formation energy ( $E_{\text{form}}$  per primitive unit cell), spin ( $\mu_S$ ) and orbital moments ( $\mu_L$ ) in both individual and total number of atoms per primitive unit cell, spin gap ( $E_g^\uparrow$ ), and carrier densities ( $\mathcal{N}$ ) at the Fermi level of FeX<sub>2</sub> monolayers within spin-polarized GGA calculations. Available experimental data from Ref. [35] on bulk FeX<sub>2</sub> lattice parameters are shown for comparison.

	$a$ (Å)		$\vartheta$ (°)	$E_{\text{form}}$ (eV)	$\mu_S^{\text{Fe}}$	$\mu_S^{\text{X}}$	$\mu_S^{\text{tot}}$	$\mu_L^{\text{Fe}}$	$\mu_L^{\text{X}}$	$\mu_L^{\text{tot}}$	$E_g^\uparrow$ (eV)	$\mathcal{N}^{\varepsilon_f}$
	DFT	Expt.			( $\mu_B$ )	( $\mu_B$ )	( $\mu_B$ )	( $\mu_B$ )	( $\mu_B$ )	( $\mu_B$ )		( $\mu_B$ )
FeCl <sub>2</sub>	3.546	3.570	91.009	-3.872	3.689	0.155	3.999	0.101	0.001	0.103	5.139	$3.842 \times 10^{13}$
FeBr <sub>2</sub>	3.745	3.740	90.076	-3.504	3.642	0.178	3.998	0.121	0.006	0.133	3.918	$4.439 \times 10^{13}$
FeI <sub>2</sub>	4.007	4.040	89.920	-3.341	3.535	0.232	3.998	0.159	0.016	0.191	3.106	$3.137 \times 10^{14}$

Table SI for other materials [33]). Moreover, the phonon dispersions also indicate real eigenfrequencies of all the branches throughout the Brillouin zone of this 1T phase [Fig. 1(b)], and there is no tendency of dynamical phase switching to stabilize their ground state configurations. This means, 1T FeX<sub>2</sub> monolayers are dynamically stable, and, thus, possible to synthesize them by simple enough experimental techniques, like exfoliation or chemical vapor deposition (CVD) or sophisticated molecular-beam epitaxy (MBE). In fact, Zhou *et al.* [34] have recently grown FeCl<sub>2</sub> using MBE and confirmed that FeCl<sub>2</sub> remains in 1T phase even in the single-layer limit. However, their study is concerned till the evaluation of material structure and stability. We also summarize the optimized lattice properties of these monolayers (Table I) and these are in-line with the previous theoretical as well as experimental reports on monolayer or bulk forms of FeX<sub>2</sub> [19,34,35]. For all the cases, one can see the Fe-X-Fe bond angles are  $\sim 90^\circ$ , whereas, the lattice constant increases with an increasing atomic radius of the halogens (Cl  $\rightarrow$  Br  $\rightarrow$  I).

We further evaluate the existence of ground-state magnetic ordering by comparing the energies of nonmagnetic (NM), ferromagnetic (FM), antiferromagnetic (AFM) (in a  $2 \times 2$  supercell), and longer range antiferromagnetic (LRAFM) configurations (e.g., up-up, down-down ordering in a  $4 \times 4$  supercell). The results indicate that the NM, AFM, and LRAFM configurations are higher in energy than the FM one (for instance,  $\sim 1.68$ ,  $\sim 0.08$ , and  $\sim 0.07$  eV/unit cell higher, respectively, for FeCl<sub>2</sub>; see Supplemental Material Table SI for other materials [33]). This means, the ferromagnetic ordering in all these FeX<sub>2</sub> monolayers is energetically favorable, which is also consistent with the prior studies [18,19]. We also compute the magnetic moments ( $\mu_S$ ) of these monolayers, including the contribution of Fe and X atoms, from their spin-polarized Mulliken populations. The result shows that  $\mu_S$  develops mainly at the Fe sites though there is a slight development on halogens due to the coordination of halides with Fe in FeX<sub>2</sub> crystal (see Table I). This happens due to the coordination (bonding mechanism) of halides with Fe atoms that basically forms a ferromagnetic super-exchange coupling between the 3d Fe atoms via nonmagnetic 2p X atoms (for a detailed description of the spin moments, see Fig. S1 of the Supplemental Material [33]). The overall  $\mu_S$  in FeX<sub>2</sub> is very close to the expected value for a Fe<sup>2+</sup> ion with four unpaired electrons ( $4\mu_B$ /unit cell). Besides, we also expect a significant development of orbital moments ( $\mu_L$ ) due to the SOC that arises from partially filled  $d$  orbitals of Fe<sup>2+</sup> ions in FeX<sub>2</sub>. Therefore, we estimate the  $\mu_L$  of FeX<sub>2</sub> monolayers including SOC in our calculations, where the Cartesian component of

$\mu_L$  on site “ $i$ ” is defined as [36]

$$\langle \mu_L^i \rangle = \text{Re} \sum_{n,k} \omega_k f_{n,k} \sum_{abc} \varrho_a^{n\dagger}(\mathbf{k}) [L_i]_{ab} \mathcal{S}_{bc}(\mathbf{k}) \varrho_c^n(\mathbf{k}), \quad (2)$$

in which  $n$  is the band index,  $\mathbf{k}$  is the wave-vector with corresponding weight  $\omega_k$ , and  $f_{n,k}$  is the occupation factor. The second sum runs over atomic orbitals centered on each site  $i$ , wherein  $\varrho_c^n$  is the eigenvector component for an orbital  $a$ , and  $L$  and  $\mathcal{S}$  denote the orbital momentum operator and orbital overlap integrals, respectively. With this formulation, the obtained  $\mu_L$  are shown in Table I. The total orbital moments of these materials are in the range of 0.1 to  $0.2\mu_B$ /unit cell in which the primary contributions come from the Fe atoms. Although these  $\mu_L$  are much smaller than the isolated Fe<sup>2+</sup> ion ( $2\mu_B$  according to Hund’s second rule), they are quite reasonable. In fact, these residual orbital moments indicate that a partial quenching of orbital moments occurs due to the strong SOC of these materials, similar to 2D Fe<sub>3</sub>GeTe<sub>2</sub> ferromagnets [37]. Interestingly, the orbital moment on Fe ion increases with the atomic radius of the halide atoms and it happens due to the superexchange coupling in FeX<sub>2</sub> crystals (explained in Supplemental Material Fig. S1(d) [33] and later in Sec. III E). It is evident from Table I that when we move to heavier halide atoms (Cl  $\rightarrow$  Br  $\rightarrow$  I), the SOC on halide atoms becomes stronger as  $\mu_L^{\text{X}}$  increases [38]. Owing to the superexchange interaction, this rise in  $\mu_L^{\text{X}}$  also increases the  $\mu_L^{\text{Fe}}$  and consequently, the overall orbital moment of FeX<sub>2</sub> (see Table I). This section, overall, ascertains that we indeed use the FeX<sub>2</sub> monolayer in its stable configuration for further calculations of their spin transport and spin-dynamical properties.

## B. Half-metallicity

We now proceed to investigate the electronic and magnetic properties of these single-layer FeX<sub>2</sub> and discuss the importance of their application in spintronics devices. Figure 2(a) shows the spin-resolved electronic band structure of FeCl<sub>2</sub>, obtained within GGA. Notably, a spin gap ( $\sim 5$  eV) already opens up in the spin-up bands, while the spin-down bands show metallic nature in the vicinity of the Fermi energy ( $\varepsilon_f$ ). Moreover, we observe that this metallic nature actually originates from the partially occupied Fe 3d orbitals [Fig. 2(b)]. Particularly, a hybridization of in-plane  $d$  orbitals ( $d_{xz}$ ,  $d_{yz}$ ,  $d_{xy}$ , and  $d_{x^2-y^2}$ ) occurs due to the super-exchange interaction between neighboring Fe atoms and contributes carriers to those metallic bands, whereas, the out-of-plane  $d_{z^2}$  orbital forms a nearly flat band very close to the Fermi level. These



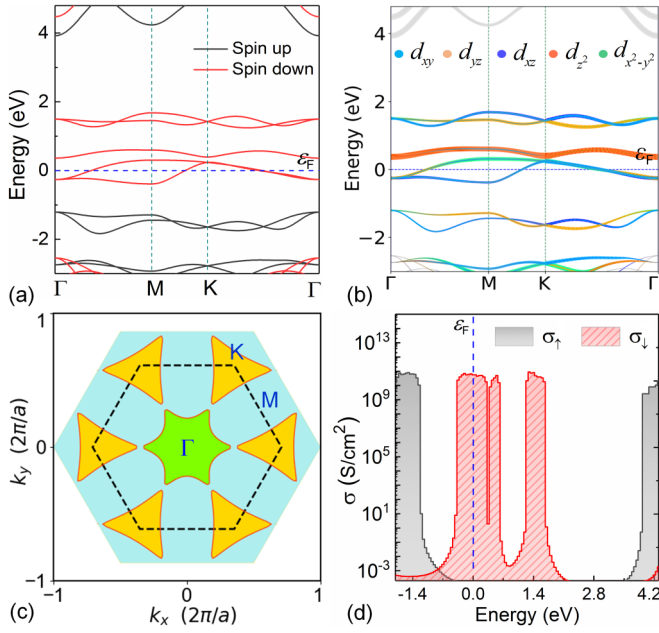


FIG. 2. (a) Spin-polarized electronic band structure and (b) corresponding fat bands of monolayer  $\text{FeCl}_2$ . (c) 2D Fermi surface of  $\text{FeCl}_2$ , comprising spin-down carriers, where the holelike pockets around  $K$  points (in yellow) belong to the lower energy band, while the electron-holelike pockets around the  $\Gamma$  (in green) point belong to upper energy band at  $\varepsilon_f$ . (d) Spin-resolved conductance of  $\text{FeCl}_2$  at the ballistic limit.

also reflect on the projected density of states (pdos) as seen in Supplemental Material Fig. S2 [33]. A similar electronic nature holds true for  $\text{FeBr}_2$  and  $\text{FeI}_2$  as well (see Figs. S3 and S4 [33], and Table I for spin gaps). It is to note that the inclusion of noncollinear SOC leads to a slight reduction of the spin gap, whereas, the spin-down states around  $\varepsilon_f$  change only marginally, and the materials remain essentially half-metallic in nature (see Supplemental Material Fig. S5 [33]). Therefore, the half-metallicity of this group of materials is completely intrinsic, which means these materials can generate fully spin-polarized carrier transport in spintronic devices.

Along with intrinsic half-metallicity, Fermi surface (FS) also plays an important role in the spin-injection or filtering efficiency in spintronic devices. Particularly, when the shape of FS of a current injection source matches with the target electrode material, the spin scattering reduces significantly and the propagating states see a very low potential barrier at the interface [39,40]. Therefore, we also analyze the FS and show it in Fig. 2(c) for  $\text{FeCl}_2$ , for instance. In the band structure plot, we notice that there are two spin-down bands that cross the Fermi level [see Fig. 2(a)]. These two bands basically form the FS of these materials. The lower energy band (at  $\varepsilon_f$ ) forms a holelike pocket around the high symmetry “ $K$ ” point (in yellow). Whereas, the higher energy band (at  $\varepsilon_f$ ) occupies the BZ except around the  $\Gamma$  and creates an electron-hole like pocket around the center of the BZ (in green), as seen in Fig. 2(c). For other iron halides too, we notice a similar type of FS (see Supplemental Material Figs. S3(c) and S4(c) [33]). Therefore, if we choose an injection source having FS very close to that of  $\text{FeX}_2$  and similar structural parameters to min-

imize lattice strain, then we can easily mitigate the effect of spin scattering and can generate a large spin-polarized current in these  $\text{FeX}_2$ -based devices. We further calculate the Fermi velocity ( $v_f$ ) across the FS in these materials following the relation,  $\hbar v_f = d\varepsilon(k)/dk$ , and find that there is a distribution in Fermi velocity (in the range of  $6.5 \times 10^4$  to  $1.3 \times 10^5$  m/s for  $\text{FeCl}_2$ ,  $2.3 \times 10^4$  to  $1.1 \times 10^5$  m/s for  $\text{FeBr}_2$ , and  $2.0 \times 10^4$  to  $1.0 \times 10^5$  m/s for  $\text{FeI}_2$ ) as a consequence of the anisotropic nature of FS in these materials. Despite this distribution, the overall values are significantly high and, thus, high mobility fully spin-polarized carriers might also be possible in these materials.

Furthermore, we calculate the spin-resolved electronic transport properties using NEGF-based carrier transport formalism in conjunction with DFT [41]. Within this framework, the spin-dependent transmission occurs across the electrodes through a finite-size scattering region and, accordingly, the conductivity of different spin channels ( $\sigma_\uparrow$  and  $\sigma_\downarrow$ ) at an energy “ $\varepsilon$ ” in the ballistic limit is defined by the Landauer formula,

$$\sigma_{\uparrow,\downarrow}(\varepsilon) = \frac{e^2}{A\pi\hbar} \int_{\text{BZ}} dk T_{\uparrow,\downarrow}(\mathbf{k}, \varepsilon), \quad (3)$$

with spin-dependent transmission probability,

$$T_{\uparrow,\downarrow}(\mathbf{k}, \varepsilon) = \text{Tr}[\Gamma_{\uparrow,\downarrow}^L(\mathbf{k}, \varepsilon) G_{\uparrow,\downarrow}^\dagger(\mathbf{k}, \varepsilon) \Gamma_{\uparrow,\downarrow}^R(\mathbf{k}, \varepsilon) G_{\uparrow,\downarrow}(\mathbf{k}, \varepsilon)], \quad (4)$$

where  $e$  is electron charge,  $\hbar$  is the reduced Planck constant, and  $A$  is area. Moreover, the integral over  $\mathbf{k}$  extends over the Brillouin zone (BZ) to comprise all the transmission modes. In Eq. (4),  $\Gamma_{\uparrow,\downarrow}^{L(R)}$  is the so-called broadening matrix associated with the self energy matrix ( $\Sigma_{\uparrow,\downarrow}^{L(R)}(\mathbf{k}, \varepsilon)$ ) of the left (right) electrode and  $G_{\uparrow,\downarrow}(\mathbf{k}, \varepsilon)$  is the retarded Green’s function ( $= [\varepsilon \mathcal{S}(\mathbf{k}) - \mathcal{H}_{\uparrow,\downarrow}(\mathbf{k}) - \Sigma_{\uparrow,\downarrow}^L(\mathbf{k}, \varepsilon) - \Sigma_{\uparrow,\downarrow}^R(\mathbf{k}, \varepsilon)]^{-1}$ ) related to the Hamiltonian ( $\mathcal{H}$ ) and the overlap ( $\mathcal{S}$ ) matrices. This procedure produces an energy-dependent conductivity of  $\text{FeX}_2$ . For instance, we show here the spin-resolved conductivity of  $\text{FeCl}_2$  in Fig. 2(d). One can notice that the conductivity around  $\varepsilon_f$  is exclusively determined by the spin-down channel with a remarkably large value ( $\sim 10^{11}$  S/cm $^2$ ), resulting from high carrier density ( $\mathcal{N}$ ) around  $\varepsilon_f$  (see  $\mathcal{N}$  in Table I). Hence, we can say that a strong metallic character at the Fermi surface is induced entirely by these spin-down carriers. Moreover, a 100% spin polarization ( $\sigma_{SP} = (\sigma_\uparrow - \sigma_\downarrow)/(\sigma_\uparrow + \sigma_\downarrow)$ ) exists over a sufficiently wide Fermi window ( $\sim 1.1$  eV). Similar to  $\text{FeCl}_2$ , the other two iron halides also have the same transport properties (see Supplemental Material Figs. S3(d) and S4(d) [33]). This implies, a perfect spin filtering can be achieved and can maintain a high tunnel magnetoresistance over a broad range of applied bias while employing these materials in MTJs. In this context, we want to mention that DFT-GGA usually underestimates the spin gap by nearly 25%–30% as compared to a hybrid functional (such as, HSE06) [19] or the experimental value. However, the band dispersions and other spin transport properties of these materials are qualitatively reasonable, particularly around the Fermi level, and the underestimate does not reform the overall trends of these results.

### C. Magnetocrystalline anisotropy

Magnetocrystalline anisotropy, originated from SOC, is a fundamental property of magnetic materials and plays a significant role in magnetic memory devices. Fundamentally, it is a prerequisite to enhance the thermal stability of long-range ferromagnetic ordering in reduced dimensions (according to the Mermin-Wagner theorem) [10,11]. At the same time, it technologically helps to determine the energy ( $E_{nv}$ ) which is required for nonvolatility of the written information as well as to regulate the critical current ( $I_c$ ) of magnetization switching in STT-MRAMs. This  $E_{nv}$  is basically proportional to the magnetocrystalline anisotropy energy ( $E_{MCA}$ ) which is nothing but the energy difference between two magnetization directions of the free layer in STT-MRAMs [24,25]. Thus, a higher uniaxial  $E_{MCA}$  can improve the stability of the written information in these devices. Meanwhile,  $I_c$  is also proportional to  $E_{MCA}$  according to the following relation [25],

$$I_c = 2\alpha \frac{\gamma e}{\mu_B \nu} E_{MCA}, \quad (5)$$

where,  $\alpha$  and  $\gamma$  are the Gilbert damping parameter and gyromagnetic ratio (mentioned in Eq. (1) also),  $\mu_B$  is the Bohr magneton, and  $\nu$  is a geometrical function depending on the spin polarization of the free layer. To reduce  $I_c$ , therefore, a low  $E_{MCA}$  is preferred which, on the other hand, is detrimental for  $E_{nv}$ . It implies, a reasonable  $E_{MCA}$  is desirable to balance both  $I_c$  and  $E_{nv}$ .

Owing to these facts, we explore the  $E_{MCA}$  of these  $\text{FeX}_2$  HMFs using “force theorem” [29,42]. Upon inclusion of SOC, “force theorem” expresses  $E_{MCA}$  as the difference of band-energies between two spin orientations for a particular projection “ $p$ ” (an atom or orbital projection) as [29,43],

$$E_{MCA} |p\rangle = \sum_{n,\mathbf{k}} f_{n,\mathbf{k}}(\theta, \varphi) \varepsilon_{n,\mathbf{k}}(\theta, \varphi) \omega_{n,\mathbf{k}}^p(\theta, \varphi) - \sum_{n,\mathbf{k}} f_{n,\mathbf{k}}(\theta_o, \varphi_o) \varepsilon_{n,\mathbf{k}}(\theta_o, \varphi_o) \omega_{n,\mathbf{k}}^p(\theta_o, \varphi_o), \quad (6)$$

in which,  $f_{n,\mathbf{k}}$  is the occupation factor for a band index  $n$  and wave vector  $\mathbf{k}$ , the spherical angle  $(\theta, \varphi)$  describes the spin orientation  $[(\theta_o, \varphi_o)$ , initial orientation],  $\varepsilon_{n,\mathbf{k}}(\theta, \varphi)$  is the corresponding band energy, and  $\omega_{n,\mathbf{k}}^p$  is the projection weight, which is

$$\omega_{n,\mathbf{k}}^p = \langle \psi_{n,\mathbf{k}} | (\mathbf{S}\mathbf{P} + \mathbf{P}\mathbf{S}) / 2 | \psi_{n,\mathbf{k}} \rangle, \quad (7)$$

with  $\psi_{n,\mathbf{k}}$  the eigenstate;  $\mathbf{S}$  the overlap matrix; and  $\mathbf{P}$  the projection matrix.  $\mathbf{P}$  is a diagonal, singular matrix with the ones in the indices corresponding to the orbitals we wish to project onto. Therefore, using this force theorem one can refine the MCA decomposition onto different atoms and orbitals and can obtain the orbital-resolved MCA energy,  $E_{MCA}^i = \sum_p E_{MCA}^i |p\rangle$  with  $p$  going over all the orbitals of the  $i$ th atom. It is worth noting that the results obtained using this theorem strongly depend on the energy dispersions near the Fermi surface, therefore, we pay special attention to the convergence of the Brillouin zone integral of the eigenvalues and perform all the calculations with a dense  $k$ -point sampling ( $35 \times 35 \times 1$ ) of the full Brillouin zone.

Interestingly, for a given  $\theta$ , we notice that the in-plane energies are isotropic (i.e., invariant with azimuthal angle

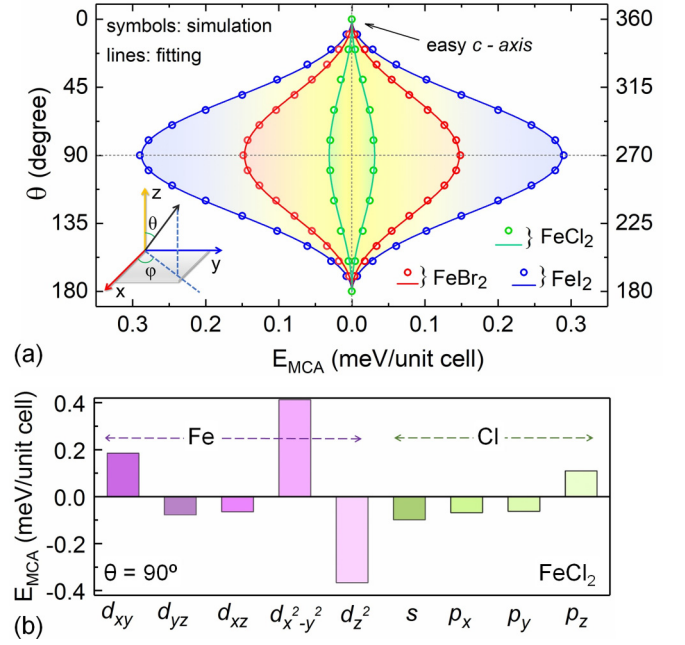


FIG. 3. (a) The variation of magnetocrystalline anisotropy energy ( $E_{MCA}$ ) with polar angle  $\theta$  in  $\text{FeX}_2$  monolayers. The symbols and lines are corresponding to the simulations and the fittings of Eq. (8), respectively. The inset shows the polar coordinates. (b) The orbital projections of  $E_{MCA}$  in  $\text{FeCl}_2$  monolayer, especially the ones with maximum contribution to the total  $E_{MCA}$ .

$\varphi$ ). However,  $E_{MCA}$  has a strong dependency on the polar angle  $\theta$  as evident from Fig. 3(a). It shows,  $E_{MCA}$  reaches its maximum when  $\theta = 90^\circ$  (keeping  $\theta_o = 0^\circ$ ), i.e., along the in-plane directions of these 2D layers ( $xy$  plane). It also shows that at  $\theta = 0^\circ$ ,  $E_{MCA}$  attains its minimum. This denotes, all these materials have an easy magnetization axis perpendicular to their 2D plane. Thus, the angular dependency of  $E_{MCA}$  is a sole function of  $\theta$ , and can be expressed as (for the hexagonal symmetry) [44],

$$E_{MCA}(\theta) = K_1 \sin^2 \theta + K_2 \sin^4 \theta, \quad (8)$$

in which  $K_1$  and  $K_2$  are the MCA coefficients. When we fit Eq. (8) to the calculated  $E_{MCA}$ , we find both  $K_1$  and  $K_2$  are positive for all these  $\text{FeX}_2$  (see Table II, the extracted  $K_1$  and  $K_2$  from the fittings are presented in terms of energy density, i.e., normalized with the cross-sectional area of the individual  $\text{FeX}_2$  monolayer). This ascertains the  $c$  axis further as the only direction of easy magnetization. It also appears that  $E_{MCA}$  substantially increases while we move to heavier

TABLE II. Extracted MCA constants ( $K_1$  and  $K_2$ ) using Eq. (8), the characteristic minimum of Gilbert damping constant ( $\alpha$ ), total exchange interactions ( $J$ ), spin-wave stiffness ( $D$ ), exchange stiffness ( $A$ ) of  $\text{FeX}_2$  monolayers.

	$K_1$ (mJ/m <sup>2</sup> )	$K_2$ (mJ/m <sup>2</sup> )	$\alpha$	$J$ (meV)	$D$ (meV.Å <sup>2</sup> )	$A$ (pJ/m)
$\text{FeCl}_2$	0.045	0.002	$7.9 \times 10^{-5}$	11.145	72.716	3.790
$\text{FeBr}_2$	0.161	0.033	$1.6 \times 10^{-4}$	8.631	71.646	3.125
$\text{FeI}_2$	0.251	0.083	$3.7 \times 10^{-4}$	4.455	50.383	1.779

halide atoms (Cl  $\rightarrow$  Br  $\rightarrow$  I) in FeX<sub>2</sub> monolayers, similar to the trend of orbital moments (discussed in Sec. III A and Table I). Moreover, from the  $x$ ,  $y$ ,  $z$  components of total orbital moments (i.e.,  $\mu_{Lx}^{\text{tot}}$ ,  $\mu_{Ly}^{\text{tot}}$ , and  $\mu_{Lz}^{\text{tot}}$ ) in Supplemental Material Table SII [33], it is clear that the anisotropy of orbital moment between out-of-plane and in-plane directions, i.e.,  $(\mu_{Lz}^{\text{tot}} - \mu_{Lx}^{\text{tot}})$  increases when we move from Cl  $\rightarrow$  Br  $\rightarrow$  I and consequently the  $E_{\text{MCA}}$  also increases, as  $E_{\text{MCA}} \sim \xi_{\text{soc}} \times (\mu_{Lz}^{\text{tot}} - \mu_{Lx}^{\text{tot}})$  according to the Bruno model, where  $\xi_{\text{soc}}$  is the SOC strength [45]. Besides, the orbital projections in Fig. 3(b) and in Supplemental Material Fig. S6 [33] strengthen the fact that  $3d_{xy}$  and  $3d_{x^2-y^2}$  orbitals of Fe primarily determine the MCA of these FeX<sub>2</sub> HMFs, which also dominate in the density of states (dos) at the Fermi level (see Supplemental Material Figs. S2–S5 [33]). Most importantly, the obtained  $E_{\text{MCA}}$  (corresponding to the difference between in-plane and off-plane directions) are quite sizable even at the ultimate body-thickness ( $\sim 3\text{\AA}$ ) of FeX<sub>2</sub> monolayers. For instance, if we compare the calculated  $E_{\text{MCA}}$  of these FeX<sub>2</sub> monolayers with the theoretical values of conventional materials like, Fe, Co, Ni (1 to 3  $\mu\text{eV}/\text{atom}$ ) [46], then  $E_{\text{MCA}}$  of these monolayers are much higher. These are also comparable to the theoretical reports of ultrathin oxides, such as CuO, (0.05 meV/f.u.), FeO (0.23 to 0.32 meV/f.u.), Fe<sub>3</sub>O<sub>4</sub> (0.23 meV/f.u.), CuFe<sub>2</sub>O<sub>4</sub> (0.24 meV/f.u.), La<sub>0.7</sub>Sr<sub>0.3</sub>MnO<sub>3</sub> (0.1 meV/f.u.), etc. [47,48], Fe-based bulk  $Ll_0$  Alloys, such as FeCu (0.20 meV/f.u.), FePd (−0.02 meV/f.u.), etc. [49], or body-centered B2 phase of FeCoN<sub>x</sub> (0 to 0.50 meV/f.u.) [50], which are vastly used as electrode materials in STT-MRAMs. Moreover, if we compare these  $E_{\text{MCA}}$  with the theoretical reports of different 2D ferromagnetic materials, like monolayer CrCl<sub>3</sub>, CrBr<sub>3</sub>, CrI<sub>3</sub> (0.02 to 0.8 meV/Cr atom) [51], VS<sub>2</sub> (0.3 meV/f.u.) [52], CrSnTe<sub>3</sub>, CrGeTe<sub>3</sub>, CrSiTe<sub>3</sub> (0.06 to 0.4 meV/f.u.) [53], CrP (0.21 meV/Cr atom), CrAs (−0.38 meV/Cr atom) [54], MnP (0.16 meV/Mn atom), MnAs (0.16 meV/Mn atom) [55], WSe<sub>2</sub>/CrGeTe<sub>3</sub> heterostructure (0.05 meV/cell) [56], then our calculations also show a similar range of values for these FeX<sub>2</sub> monolayers. The calculated  $E_{\text{MCA}}$  energies are also comparable or relatively higher than the experimental values of CrCl<sub>3</sub> (0.08 to 0.1 meV/Cr atom) [57] and Fe monolayer/Rh(111) (0.08 meV/Fe atom), Co monolayer/Pt (111) (0.1 meV/Co atom) systems [58]. Further, in the case of STT-MRAM, Liu *et al.* [59] experimentally shows that a 1.1 nm CoFeB thin-film (with diameter 50 nm) on 2 nm Tungsten has an effective perpendicular magnetic anisotropy of 0.29 mJ/m<sup>2</sup> and that produces a thermal stability factor of 137 which is beyond the requirement (stability factor  $> 67$  [60]) of 10-year data retention of an STT-MRAM. A similar anisotropy (0.27 mJ/m<sup>2</sup>) is also reported by Ikeda *et al.* [25] for a CoFeB of 1.6 nm thickness and 40 nm diameter based STT-MRAM. Our simulated MCA values of these FeX<sub>2</sub> monolayers are quite close to these values, particularly for FeI<sub>2</sub> monolayer (see K<sub>1</sub> in Table II). This also suggests the potential of FeX<sub>2</sub> monolayers in ultrathin spin memory devices.

#### D. Gilbert damping

Gilbert damping ( $\alpha$ ), like MCA, is also an important consequence of SOC and another crucial factor to determine

the performance of different magnetic materials and devices. As mentioned in Eq. (5), the critical current ( $I_c$ ) of a STT-MRAM is also proportional to  $\alpha$ . This implies, an electrode material with a small  $\alpha$  can lower the power consumption of these devices. Besides, in magnetic thin-film microwave devices, a low  $\alpha$  sharpens the ferromagnetic resonance (FMR) (linewidth,  $\Delta H \propto \alpha$ ) [61], and also allows the spin-waves to propagate over substantial distances in magnonic devices [62]. Therefore, a detailed understanding of  $\alpha$  would greatly facilitate the design of these FeX<sub>2</sub> ferromagnets for a variety of applications.

Here, we calculate the Gilbert damping in the framework of Kambersky's torque-torque correlation model which was further extended by Gilmore *et al.* [63] and Thonig *et al.* [64,65]. Particularly, we focus on calculating the damping tensor with elements,

$$\alpha_{pq} = \frac{g}{\mu_S^{\text{tot}} \pi} \sum_{\mathbf{k}} \omega_{\mathbf{k}} \sum_{n,m} \mathcal{W}_{n,m}(\mathbf{k}) \mathcal{T}_{n,m}^q(\mathbf{k}) [\mathcal{T}_{n,m}^p(\mathbf{k})]^\dagger, \quad (9)$$

where  $g$  is the Landé  $g$ -factor,  $\mu_S^{\text{tot}}$  is the total magnetic moment, and  $p, q = x, y, z$ . The first sum is over  $\mathbf{k}$  with corresponding weight  $\omega_{\mathbf{k}}$  in the Brillouin zone, whereas the second one runs over the band indices,  $n, m$ .  $\mathcal{T}_{n,m}^p(\mathbf{k}) = \langle n, \mathbf{k} | \mathcal{T}^p | m, \mathbf{k} \rangle$  are the matrix elements of the torque operator  $\mathcal{T} = [\sigma, \mathcal{H}_{SO}]$ , wherein  $\sigma$  and  $|n, \mathbf{k}\rangle$  are the Pauli spin matrices and Bloch eigenstate of the spin-orbit Hamiltonian  $\mathcal{H}_{SO}$ , respectively. Besides, the spectral overlap function,  $\mathcal{W}_{n,m}(\mathbf{k})$ , between two bands  $\varepsilon_{n,\mathbf{k}}$  and  $\varepsilon_{m,\mathbf{k}}$  is defined as

$$\mathcal{W}_{n,m}(\mathbf{k}) = \int \mathcal{F}(\varepsilon) A_{n,\mathbf{k}}(\varepsilon, \Lambda) A_{m,\mathbf{k}}(\varepsilon, \Lambda) d\varepsilon, \quad (10)$$

where  $\mathcal{F}(\varepsilon)$  is the negative derivative of the Fermi-Dirac distribution function, and  $A_{n,\mathbf{k}}(\varepsilon, \Lambda) = (1/\pi)[\Lambda/((\varepsilon_{n,\mathbf{k}} - \varepsilon)^2 + \Lambda^2)]$  defines a Lorentzian spectral function with life-time broadening  $\Lambda$ . This  $\Lambda$  is basically a phenomenological account of electron-phonon scattering process. Note that there can be other possible origins of this  $\Lambda$  as well, such as impurity scattering, alloy scattering, or even spin-dependent scattering process [66]; however, we can assume, electron-phonon scattering mechanism is the dominant one in a pure crystalline structure, at least for temperatures  $T > 0$  K. Therefore, we calculate here the damping matrices for a range of lifetime broadening to depict the variation of  $\alpha_{pq}$  with scattering rate. Although this electron-scattering mechanism has a physical dependency on temperature, it is worth noting that we treat here the average  $\Lambda$  as an independent parameter, and consider the explicit temperature dependency of  $\alpha_{pq}$  solely through  $\mathcal{F}(\varepsilon)$  in Eq. (10) [64,67]. Besides, we again choose a dense  $k$ -mesh ( $35 \times 35 \times 1$ ) of the Brillouin zone to ensure the convergence of  $\alpha_{pq}$ , just like MCA.

In Fig. 4(a), we present the tensor elements  $\alpha_{pp}$  of FeX<sub>2</sub> versus the broadening parameter  $\Lambda$ . As FeX<sub>2</sub> has hexagonal symmetry, the damping tensor is a diagonal one as the off-diagonal elements are almost negligible. Along with this, the in-plane components ( $\alpha_{xx} = \alpha_{yy}$ ) are found to be dominant as compared to the out-of-plane component,  $\alpha_{zz}$ . Interestingly, the in-plane components produce a unique minimum in damping constant (around  $\Lambda = 0.02$  to  $0.03$  eV), as commonly seen in bulk ferromagnets like Fe, Co, and Ni or their ultrathin layers (obtained by *ab initio* calculations) [63–68]. Gener-



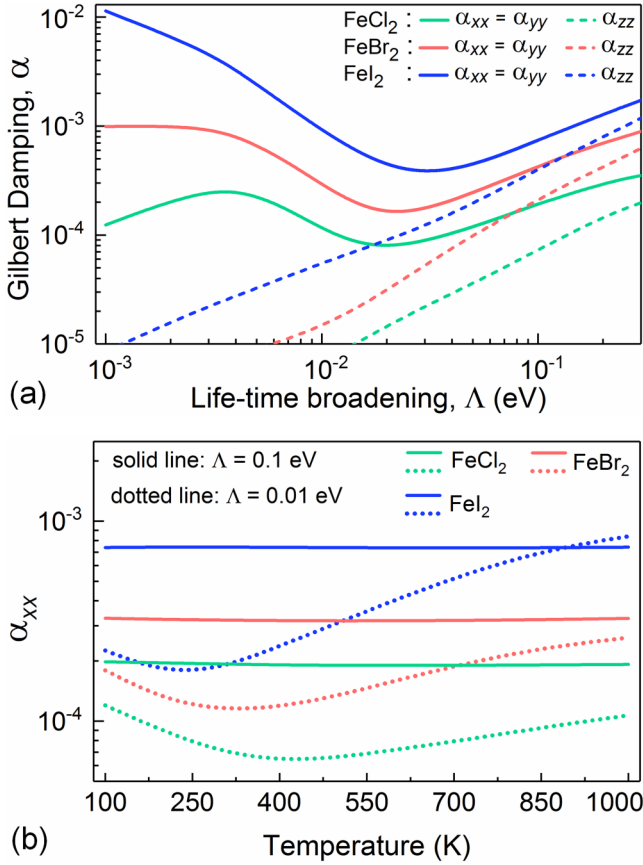


FIG. 4. (a) Gilbert damping tensors of monolayer FeX<sub>2</sub> HMFs as a function of spectral broadening  $\Lambda$ . Here,  $\alpha_{xx} = \alpha_{yy} \neq \alpha_{zz}$ , as FeX<sub>2</sub> monolayers have hexagonal symmetry. (b) Temperature variation of  $\alpha_{xx}$  for two fixed spectral broadenings  $\Lambda = 0.01$  and  $0.1$  eV, respectively.

ally, this characteristic minimum appears due to the dominant intra- and interband transitions that occur at the small and large  $\Lambda$  regions, respectively. For a small  $\Lambda$ , the overlap of the spectral functions is less and thus, a strong intraband transition within a single energy band [i.e.,  $n = m$  in Eq. (9)] leads to a conductivity-like term in damping. In contrast, the broad spectral overlap in high  $\Lambda$  region increases the interband transition [i.e.,  $n \neq m$  in Eq. (9)] that surpasses the intra-band transition and leads to a resistivity-like term in damping. These fundamental transitions also suggest that Gilbert damping is a Fermi surface effect and varies with the total density of states at the Fermi level [ $n(\varepsilon_f)$ ]. Typically, it shows a dependency like  $\alpha \propto \xi_{\text{soc}}^2 n(\varepsilon_f)$  [65,67,69]. This phenomenon is also found in these FeX<sub>2</sub> HMFs. When moving toward heavier halide atoms, both  $n(\varepsilon_f)$  and  $\xi_{\text{soc}}$  increase in accordance with the increase in carrier densities ( $\mathcal{N}$ ) and orbital moments ( $\mu_L^{\text{tot}}$ ), respectively (see Table I). As a consequence,  $\alpha_{pp}$  increases with Cl  $\rightarrow$  Br  $\rightarrow$  I which is depicted in Fig. 4(a).

We further check the effect of electron temperature on  $\alpha_{xx}$  and show it for a high and a low life-time broadenings,  $\Lambda = 0.1$  and  $0.01$  eV, for instance [see Fig. 4(b)]. As stated earlier, we examine this by incorporating the temperature via  $\mathcal{F}(\varepsilon)$  in Eq. (10). It shows,  $\alpha_{xx}$  is barely sensitive to temperature at  $\Lambda = 0.1$  eV. This is quite certain, since the spectral functions

( $A_{n,k}$ ) already dominate over  $\mathcal{F}(\varepsilon)$  in Eq. (9). On the contrary, when the broadening is considerably less (i.e.,  $\Lambda = 0.01$  eV), the calculated  $\alpha_{xx}$  varies notably with temperature and forms again a characteristic minimum. In the low temperature region (left to the characteristic minimum), the intra-band transition basically dominates and decreases  $\alpha_{xx}$  with increase in temperature (discussed earlier). While, at high temperature region (right to the characteristic minimum), the spectral overlap increases due to the extended Fermi distributions which eventually increases  $\alpha_{xx}$  with temperature [64,70].

From this overall analysis, we can say that these insights will help to understand the experimental Gilbert damping constants of these materials as well as other 2D materials, in future. We further emphasize that the calculated Gilbert damping of these half-metallic FeX<sub>2</sub> monolayers are smaller (the characteristic minimum is in the range of  $7.9 \times 10^{-5}$  to  $3.7 \times 10^{-4}$ ; see Table II) due to their relatively low  $n(\varepsilon_f)$  than the normal ferromagnetic metals where both spin-channels are active. Moreover, we compare these calculated  $\alpha$  of FeX<sub>2</sub> monolayers with different other classes of materials (both theoretical and experimental values) and present in Fig. S7 of the Supplemental Material [33] (see, also, Refs. [7,63,71–84] therein). From Fig. S7, it is evident that the Gilbert damping values of FeX<sub>2</sub> monolayers are much lower than the conventional materials (like Fe, Co, Ni) or different permalloys (like CoFeB, NiFe, etc.) which have  $\alpha > 10^{-3}$ . Moreover, these values are also lower/comparable to the other half-metallic oxides (such as CrO<sub>2</sub>, La<sub>0.7</sub>Sr<sub>0.3</sub>MnO<sub>3</sub>) or Heusler alloy (such as Co<sub>2</sub>MnSi, Co<sub>2</sub>MnGe, Co<sub>2</sub>FeSi, etc.) thin films. It is noticeable that these values are also closer to the experimental reports of ferrimagnetic insulator, Y<sub>3</sub>Fe<sub>5</sub>O<sub>12</sub>, which is the magnetic material with the lowest known Gilbert damping constant [85]. Therefore, the achieved Gilbert damping constants are relatively low for these materials, and, thereby, these 2D HMFs can diminish power consumption in STT-MRAM devices.

### E. Exchange interactions

Along with the properties we have discussed so far, exchange interaction is also a crucial parameter that governs the exchange and correlation length of exchange bias, topological spin textures, as well as the robustness of ordered magnetic states against thermal fluctuations. Most importantly, the thermal stability and critical current ( $I_c$ ) of magnetization switching in STT-MRAM are also very sensitive to the exchange stiffness constant ( $\mathcal{A}$ ) of the free layer [86] that is related to the exchange interaction. Therefore, quantifying the exchange interaction is also essential for these FeX<sub>2</sub> monolayers.

To illustrate the effective exchange interaction, we adopt the intersite spins according to the Heisenberg Hamiltonian,

$$\mathcal{H}_{\text{EXC}} = - \sum_{i \neq j} J_{ij} \mathbf{S}_i \cdot \mathbf{S}_j, \quad (11)$$

where  $J_{ij}$  is the effective exchange-coupling constant between spins  $\mathbf{S}_i$  and  $\mathbf{S}_j$  located at site  $i$  and  $j$ , respectively. Consequently, a positive (negative) sign of  $J_{ij}$  indicates a ferromagnetic (anti-ferromagnetic) coupling between two spins. To estimate this  $J_{ij}$ , we consider the Green's function-based

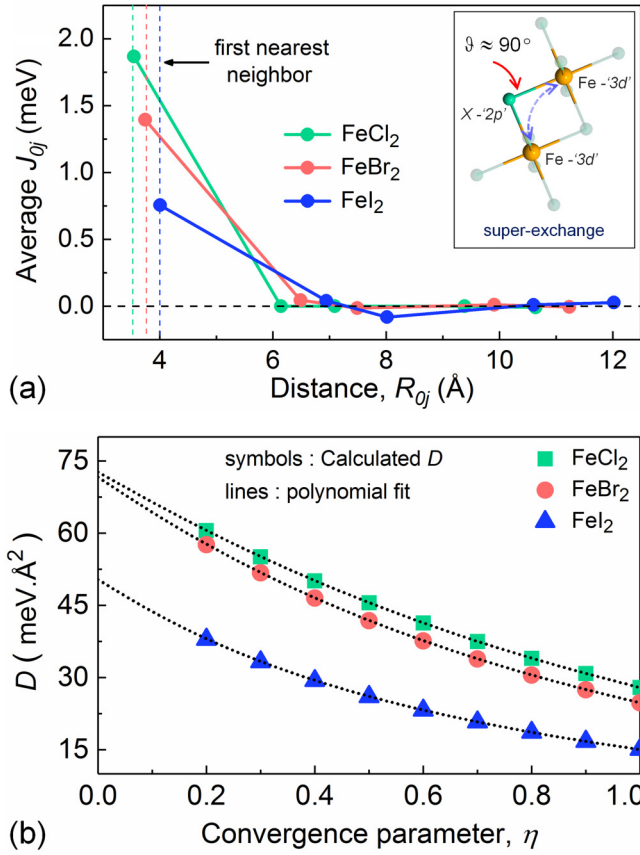


FIG. 5. (a) Dependence of exchange interaction ( $J_{0j}$ ) on the distance between Fe sites ( $R_{0j}$ ) in FeX<sub>2</sub> monolayers. (b) Spin-wave stiffness constant  $D(\eta)$  as a function of the convergence parameter  $\eta$  along with a fifth order polynomial fit used to extrapolate  $D$  at  $\eta = 0$ .

LKAG (Liechtenstein, Katsnelson, Antropov, and Gubanov) formalism, as prescribed by Liechtenstein *et al.* [87], which is known to be more realistic for first-principle calculations of  $J_{ij}$ . Within this formalism, we can define  $J_{ij}$  as [88]

$$J_{ij} = (1/2\pi) \int_{-\infty}^{\epsilon_f} \text{Tr}[\hat{G}_{ij}^\uparrow \hat{V}_j \hat{G}_{ji}^\downarrow \hat{V}_i] d\epsilon, \quad (12)$$

where  $\hat{G}_{ij}^{\uparrow\downarrow}$  denotes the intersite Green's function operator between sites  $i$  and  $j$ , and  $\hat{V}_i$  is the on-site exchange splitting at site  $i$ . We further state that, we calculate  $J_{ij}$  between pairs of local magnetic moments of Fe ions as they contribute mainly to the magnetic moments of FeX<sub>2</sub> (explained in Sec. III A with values shown in Table I). Moreover, we consider a cell repetition of  $9 \times 9 \times 1$  to realize the long-range variation of  $J_{ij}$  over an interatomic distance ( $R_{ij}$ ) up to the fifth nearest-neighbor, at least. Figure 5(a) shows the variation of  $J_{0j}$  (averaged over the number of atoms on each shell of nearest neighbors ( $n_{NN}$ ) of atom  $i = 0$ ) with  $R_{0j}$  ( $= |\mathbf{R}_0 - \mathbf{R}_j|$ ). This brings out that the exchange interaction is relatively short-ranged. It decreases sharply after the first nearest neighbor and thereafter follows a very weak oscillatory nature, similar to the Ruderman-Kittel-Kasuya-Yoshida (RKKY) interaction [89]. We also list the total  $J$  ( $= \sum_j n_{NN}^j J_{0j}$ ) in Table II, which are all positive for these FeX<sub>2</sub> monolayers and indicative of

the overall ferromagnetic ordering. This is indeed consistent with the fact of ferromagnetic super-exchange coupling that occurs between the 3d states of consecutive Fe atoms via the nonmagnetic  $p$  states of X [see Fig. 5(a) inset], in accordance with the Goodenough-Kanamori-Anderson (GKA) rule [90].

From this exchange interaction, we evaluate the spin-wave stiffness,  $D$ . In the long-wavelength limit of spin-wave energy of a uniform 2D ferromagnet, we can approximate it as [87,91]

$$D = \lim_{\eta \rightarrow 0} D(\eta), \quad (13)$$

$$D(\eta) = \sum_j \frac{2\mu_B}{\mu_S} J_{0j} R_{0j}^2 \exp\left(-\eta \frac{R_{0j}}{R_{01}}\right), \quad (14)$$

where  $R_{01}$  is the first nearest-neighbor interatomic distance. To ensure the convergence of the sum in Eq. (14), we use a convergence parameter  $\eta$  and estimate  $D$  under the limit of  $\eta \rightarrow 0$  [91,92]. We, therefore, extend the  $\sum_j$  over a sufficiently large distance to calculate  $D(\eta)$  (in a range  $\eta \in [0.2, 1]$  which is conveniently used in the literature [91,92]), and determine  $D$  by extrapolating  $D(\eta)$  at  $\eta = 0$  [see Fig. 5(b)]. The values of  $D$  are listed in Table II along with the exchange stiffness constant  $\mathcal{A}$ , which is closely related to  $D$  via the relation,  $\mathcal{A} = (DM_s/2g\mu_B)$ , where  $M_s$  is the magnetization per unit cell [92]. From Table II, one can notice that  $\mathcal{A}$  decreases with increasing halide size in FeX<sub>2</sub>. Still, the overall  $\mathcal{A}$  are comparable to nickel, permalloy thin films [93,94], and also to the experimental values of Yttrium Iron Garnet [95]. We further estimate the Curie temperature ( $T_C$ ) of these monolayers. We use two different approaches to evaluate  $T_C$ . The first one is the commonly used Ising model ( $T_C^{\text{IM}}$ ) for a crystal having uniaxial anisotropy and the second one is based on nonlinear spin-wave theory ( $T_C^{\text{SWT}}$ ). Usually, the Ising model overshoots the experimental  $T_C$  whereas the spin-wave theory underestimates it [96]. Therefore, we can estimate an upper and lower bound of  $T_C$  using these two approaches. For a 2D triangular lattice, we can express  $T_C^{\text{IM}}$  as [97]

$$T_C^{\text{IM}} = \frac{4}{\ln(3)} \left(\frac{J}{k_B}\right) \quad (15)$$

and  $T_C^{\text{SWT}}$  as [96]

$$T_C^{\text{SWT}} = \frac{\pi JS^2}{k_B [2 \log\left(\frac{E_{\text{MCA}} + 2\pi JS}{E_{\text{MCA}}}\right)]}, \quad (16)$$

where  $k_B$  is the Boltzmann constant and spin  $S = 2$ . From Eqs. (15) and (16), the derived  $T_C^{\text{IM}}$  ( $T_C^{\text{SWT}}$ ) values are 470(222), 364(220), and 188(143) K for FeCl<sub>2</sub>, FeBr<sub>2</sub>, and FeI<sub>2</sub> monolayers, respectively, which are much higher than the prototypical 2D ferromagnets like CrI<sub>3</sub>, CrSiTe<sub>3</sub>, etc. [96,98]. As there is no experimental report yet, we can expect that the experimental  $T_C$  of these monolayers will be in between these two values and can also possibly be improved by suitable external stimuli like strain, doping or electric field, as suggested in Ref. [98].

#### IV. CONCLUSION

In summary, we systematically investigate the intrinsic spin transport and spin-dynamical properties of FeX<sub>2</sub> mono-



layers for their potential applications as spin electrodes in next-generation spin logic and memory devices. As the performance of a spin-based device largely depends on the choice of electrode materials, it is necessary that the material should have the ability to generate pure spin current, high spin injection efficiency as well as low spin leakage over a sufficiently wide bias window. Moreover, the material should have sizable perpendicular MCA, low Gilbert damping, and reasonable spin stiffness to optimize the thermal stability and critical current of the nanoscale spintronics devices. From this perspective, our results collectively show that FeX<sub>2</sub> monolayers will be right choice for spin electrodes. Particularly, the intrinsic half metallicity with a large spin gap ( $>3$  eV), high Fermi velocity ( $\sim 10^5$  m/s), high spin conductance ( $\sim 10^{11}$  S/cm<sup>2</sup>) over a wide Fermi window ( $>1$  eV), as well as low Gilbert damping ( $7.9 \times 10^{-5}$  to  $3.7 \times 10^{-4}$ ), sizable uniaxial MCA (0.04 to 0.25 mJ/m<sup>2</sup>), and spin stiffness constants (50

to 70 meV.Å<sup>2</sup>) of these materials are well suited in designing ultrathin spintronics devices. Moreover, within this FeX<sub>2</sub> family, if we further analyze the impact of halides, our calculations indicate that FeCl<sub>2</sub> is a better choice in terms of the spin gap, Gilbert damping, spin stiffness, and Curie temperature, though it has a lower anisotropy in this series. However, the anisotropy is still adequate for low power spintronics devices at the monolayer limit.

#### ACKNOWLEDGMENTS

This work was supported by DST Nanomission (Grant No. DST/NM/NT/2018/89), SERB Early Career Research Award (Grant No. ECR/2018/000439), and DST INSPIRE Faculty Award (Grant No. IFA17-ENG206), Government of India.

- 
- [1] B. Hu, K. Moges, Y. Honda, H. X. Liu, T. Uemura, M. Yamamoto, J. I. Inoue, and M. Shirai, *Phys. Rev. B* **94**, 094428 (2016).
- [2] Y. Shen, D. Kan, I.-C. Lin, M.-W. Chu, I. Suzuki, and Y. Shimakawa, *Appl. Phys. Lett.* **117**, 042408 (2020).
- [3] I. Žutić, J. Fabian, S. D. Sarma, *Rev. Mod. Phys.* **76**, 323 (2004).
- [4] H. Liu, Y. Honda, T. Taira, K. Matsuda, M. Arita, T. Uemura, and M. Yamamoto, *Appl. Phys. Lett.* **101**, 132418 (2012).
- [5] A. Hirohata, K. Yamada, Y. Nakatani, I. Prejbeanu, B. Diény, P. Pirro, and B. Hillebrands, *J. Magn. Magn. Mater.* **509**, 166711 (2020).
- [6] R. Farshchi and M. Ramsteiner, *J. Appl. Phys.* **113**, 191101 (2013).
- [7] Z. Zhang, M. Cheng, Z. Yu, Z. Zou, Y. Liu, J. Shi, Z. Lu, and R. Xiong, *Phys. Rev. B* **102**, 014454 (2020).
- [8] A. Sugawara, T. Akashi, M. A. Kassem, Y. Tabata, T. Waki, and H. Nakamura, *Phys. Rev. Materials* **3**, 104421 (2019).
- [9] M. R. Li, M. Retuerto, Z. Deng, P. W. Stephens, M. Croft, Q. Huang, H. Wu, X. Deng, G. Kotliar, J. Sánchez-Benítez, J. Hadermann, D. Walker, and M. Greenblatt, *Angew. Chemie Int. Ed.* **54**, 12069 (2015).
- [10] N. D. Mermin and H. Wagner, *Phys. Rev. Lett.* **17**, 1133 (1966).
- [11] B. Huang, G. Clark, E. Navarro-Moratalla, D. R. Klein, R. Cheng, K. L. Seyler, D. Zhong, E. Schmidgall, M. A. McGuire, D. H. Cobden, W. Yao, D. Xiao, P. Jarillo-Herrero, and X. Xu, *Nature* **546**, 270 (2017).
- [12] C. Gong, L. Li, Z. Li, H. Ji, A. Stern, Y. Xia, T. Cao, W. Bao, C. Wang, Y. Wang, Z. Q. Qiu, R. J. Cava, S. G. Louie, J. Xia, and X. Zhang, *Nature* **546**, 265 (2017).
- [13] M. Bonilla, S. Kolekar, Y. Ma, H. C. Diaz, V. Kalappattil, R. Das, T. Eggers, H. R. Gutierrez, M. H. Phan, and M. Batzill, *Nat. Nanotechnol.* **13**, 289 (2018).
- [14] D. J. O'Hara, T. Zhu, A. H. Trout, A. S. Ahmed, Y. K. Luo, H. Lee, M. R. Brenner, S. Rajan, J. A. Gupta, D. W. McComb, and R. K. Kawakami, *Nano Lett.* **18**, 3125 (2018).
- [15] T. Song, X. Cai, M. W. Y. Tu, X. Zhang, B. Huang, N. P. Wilson, K. L. Seyler, L. Zhu, T. Taniguchi, K. Watanabe, M. A. McGuire, D. H. Cobden, D. Xiao, W. Yao, and X. Xu, *Science* **360**, 1214 (2018).
- [16] C. Jiang, Y. Wang, Y. Zhang, H. Wang, Q. Chen, and J. Wan, *J. Phys. Chem. C* **122**, 21617 (2018).
- [17] T. Cao, Z. Li, and S. G. Louie, *Phys. Rev. Lett.* **114**, 236602 (2015).
- [18] E. Torun, H. Sahin, S. K. Singh, and F. M. Peeters, *Appl. Phys. Lett.* **106**, 192404 (2015).
- [19] M. Ashton, D. Gluhovic, S. B. Sinnott, J. Guo, D. A. Stewart, and R. G. Hennig, *Nano Lett.* **17**, 5251 (2017).
- [20] V. V. Kulish and W. Huang, *J. Mater. Chem. C* **5**, 8734 (2017).
- [21] M. A. McGuire, *Crystals* **7**, 121 (2017).
- [22] T. L. Gilbert, *Phys. Rev.* **100**, 1243 (1955); *IEEE Trans. Magn.* **40**, 3443 (2004).
- [23] B. Heinrich and J. F. Cochran, *Adv. Phys.* **42**, 523 (1993).
- [24] B. Diény and M. Chshiev, *Rev. Mod. Phys.* **89**, 025008 (2017).
- [25] S. Ikeda, K. Miura, H. Yamamoto, K. Mizunuma, H. D. Gan, M. Endo, S. Kanai, J. Hayakawa, F. Matsukura, and H. Ohno, *Nat. Mater.* **9**, 721 (2010).
- [26] N. Romming, A. Kubetzka, C. Hanneken, K. von Bergmann, and R. Wiesendanger, *Phys. Rev. Lett.* **114**, 177203 (2015).
- [27] D. C. Ralph and M. D. Stiles, *J. Magn. Magn. Mater.* **320**, 1190 (2008).
- [28] H. L. Wang, C. H. Du, Y. Pu, R. Adur, P. C. Hammel, and F. Y. Yang, *Phys. Rev. Lett.* **112**, 197201 (2014).
- [29] S. Smidstrup, T. Markussen, P. Vancaeyveld, J. Wellendorff, J. Schneider, T. Gunst, B. Verstichel, D. Stradi, P. A. Khomyakov, U. G. Vej-Hansen, M. E. Lee, S. T. Chill, F. Rasmussen, G. Penazzi, F. Corsetti, A. Ojanperä, K. Jensen, M. L. N. Palsgaard, U. Martinez, A. Blom, M. Brandbyge, and K. Stokbro, *J. Phys.: Condens. Matter* **32**, 015901 (2020).
- [30] M. Schlipf and F. Gygi, *Comput. Phys. Commun.* **196**, 36 (2015).
- [31] K. Choudhary, I. Kalish, R. Beams, and F. Tavazza, *Sci. Rep.* **7**, 5179 (2017).
- [32] R. K. Ghosh and S. Mahapatra, *IEEE J. Electron Devices Soc.* **1**, 175 (2013).
- [33] See Supplemental Material at <http://link.aps.org/supplemental/10.1103/PhysRevB.103.054409> for the details of energy difference in different phases, spin moment analysis, electronic band structure, projected density of states (pdos), 2D Fermi surface,

- ballistic conductance, electronic band structure, and pdos, including SOC,  $x$ ,  $y$ ,  $z$  components of orbital angular moments, Gilbert damping benchmarking plot.
- [34] X. Zhou, B. Brzostowski, A. Durajski, M. Liu, J. Xiang, T. Jiang, Z. Wang, S. Chen, P. Li, Z. Zhong, A. Drzewiński, M. Jarosik, R. Szczśniak, T. Lai, D. Guo, and D. Zhong, *J. Phys. Chem. C* **124**, 9416 (2020).
- [35] R. W. G. Wyckoff, *Crystal Structures*, 2nd ed. (Wiley, New York, 1963), Vol. I, pp. 239–444.
- [36] G. Autes, C. Barreateau, and D. Spanjaard, and M. C. Desjonqueres, *J. Phys.: Condens. Matter* **18**, 6785 (2006).
- [37] H. L. Zhuang, P. R. C. Kent, and R. G. Hennig, *Phys. Rev. B* **93**, 134407 (2016).
- [38] G. L. McPherson, R. C. Koch, and G. D. Stucky, *J. Chem. Phys.* **60**, 1424 (1974).
- [39] V. M. Karpan, G. Giovannetti, P. A. Khomyakov, M. Talanana, A. A. Starikov, M. Zwierzycki, J. vandenBrink, G. Brocks, and P. J. Kelly, *Phys. Rev. Lett.* **99**, 176602 (2007).
- [40] T. Harada, I. Ohkubo, M. Lippmaa, Y. Sakurai, Y. Matsumoto, S. Muto, H. Koinuma, and M. Oshima, *Phys. Rev. Lett.* **109**, 076602 (2012).
- [41] D. Stradi, U. Martinez, A. Blom, M. Brandbyge, and K. Stokbro, *Phys. Rev. B* **93**, 155302 (2016).
- [42] G. H. O. Daalderop, P. J. Kelly, and M. F. H. Schuurmans, *Phys. Rev. B* **41**, 11919 (1990).
- [43] D. Li, C. Barreateau, M. R. Castell, F. Silly, and A. Smogunov, *Phys. Rev. B* **90**, 205409 (2014).
- [44] R. C. O’Handley, *Modern Magnetic Materials: Principles and Applications*, 1st ed. (Wiley-Interscience, New York, 2006).
- [45] P. Bruno, *Phys. Rev. B* **39**, 865(R) (1989).
- [46] S. V. Halilov, A. Ya. Perlov, P. M. Oppeneer, A. N. Yaresko, and V. N. Antonov, *Phys. Rev. B* **57**, 9557 (1998).
- [47] D. Odkhuu, T. Tsevelmaa, D. Sangaa, N. Tsogbadrakh, S. H. Rhim, and S. C. Hong, *Phys. Rev. B* **98**, 094408 (2018).
- [48] Z. Liao, M. Huijben, Z. Zhong, N. Gauquelin, S. Macke, R. J. Green, S. Van Aert, J. Verbeeck, G. Van Tendeloo, K. Held, G. A. Sawatzky, G. Koster, and G. Rijnders, *Nat. Mater.* **15**, 425 (2016).
- [49] M. Blanco-Rey, J. I. Cerda, and A. Arnau, *New J. Phys.* **21**, 073054 (2019).
- [50] D. Odkhuu and S. C. Hong, *Phys. Rev. Appl.* **11**, 054085 (2019).
- [51] L. Webster and J. A. Yan, *Phys. Rev. B* **98**, 144411 (2018).
- [52] H. L. Zhuang and R. G. Hennig, *Phys. Rev. B* **93**, 054429 (2016).
- [53] H. L. Zhuang, Y. Xie, P. R. C. Kent, and P. Ganesh, *Phys. Rev. B* **92**, 035407 (2015).
- [54] A. Ma, P. Wang, and C. Zhang, *Nanoscale* **12**, 5464 (2020).
- [55] B. Wang, Y. Zhang, L. Ma, Q. Wu, Y. Guo, X. Zhang, and J. Wang, *Nanoscale* **11**, 4204 (2019).
- [56] B. Marfoua and J. Hong, *Nanotech.* **31**, 425702 (2020).
- [57] A. Bedoya-Pinto, J. Ji, A. Pandeya, P. Gargiani, M. Valvidares, P. Sessi, F. Radu, K. Chang, and S. Parkin, [arXiv:2006.07605v1](https://arxiv.org/abs/2006.07605v1).
- [58] A. Lehnert, S. Denmler, P. Blonski, S. Rusponi, M. Etzkorn, G. Moulas, P. Bencok, P. Gambardella, H. Brune, and J. Hafner, *Phys. Rev. B* **82**, 094409 (2010).
- [59] Y. Liu, T. Yu, Z. Zhu, H. Zhong, K. M. K., and K. Zhu, *J. Magn. Mater.* **410**, 123 (2016).
- [60] B. Tudu and A. Tiwari, *Vacuum* **146**, 329 (2017).
- [61] B. Heinrich, Y. Tserkovnyak, G. Woltersdorf, A. Brataas, R. Urban, and G. E. W. Bauer, *Phys. Rev. Lett.* **90**, 187601 (2003).
- [62] B. Lenk, H. Ulrichs, F. Garbs, and M. Münzenberg, *Phys. Rep.* **507**, 107 (2011).
- [63] K. Gilmore, Y. U. Idzerda, and M. D. Stiles, *Phys. Rev. Lett.* **99**, 027204 (2007).
- [64] D. Thonig and J. Henk, *New J. Phys.* **16**, 013032 (2014).
- [65] D. Thonig, Y. Kvashnin, O. Eriksson, and M. Pereiro, *Phys. Rev. Materials* **2**, 013801 (2018).
- [66] K. Gilmore, I. Garate, A. H. MacDonald, and M. D. Stiles, *Phys. Rev. B* **84**, 224412 (2011).
- [67] E. Barati, M. Cinal, D. M. Edwards, and A. Umerski, *Phys. Rev. B* **90**, 014420 (2014).
- [68] Y. S. Hou and R. Q. Wu, *Phys. Rev. Appl.* **11**, 054032 (2019).
- [69] F. Pan, J. Chico, J. Hellsvik, A. Delin, A. Bergman, and L. Bergqvist, *Phys. Rev. B* **94**, 214410 (2016).
- [70] S. Mankovsky, D. Ködderitzsch, G. Woltersdorf, and H. Ebert, *Phys. Rev. B* **87**, 014430 (2013).
- [71] S. Klingler, H. Maier-Flaig, C. Dubs, O. Surzhenko, R. Gross, H. Huebl, S. T. B. Goennenwein, and M. Weiler, *Appl. Phys. Lett.* **110**, 092409 (2017).
- [72] Y. Kajiwara, K. Harii, S. Takahashi, J. Ohe, K. Uchida, M. Mizuguchi, H. Umezawa, H. Kawai, K. Ando, K. Takanashi, S. Maekawa, and E. Saitoh, *Nature* **464**, 262 (2010).
- [73] F. J. Yang and X. Q. Chen, *Appl. Phys. Lett.* **102**, 252407 (2013).
- [74] C. Sterwerf, S. Paul, B. Khodadadi, M. Meinert, J.-M. Schmalhorst, M. Buchmeier, C. K. A. Mewes, T. Mewes, and G. Reiss, *J. Appl. Phys.* **120**, 083904 (2016).
- [75] B. Pradines, R. Arras, I. Abdallah, N. Biziere, and L. Calmels, *Phys. Rev. B* **95**, 094425 (2017).
- [76] C. Liu, C. K. A. Mewes, M. Chshiev, T. Mewes, and W. H. Butler, *Appl. Phys. Lett.* **95**, 022509 (2009).
- [77] L. Chen, S. Mankovsky, S. Wimmer, M. A. W. Schoen, H. S. Korner, M. Kronseder, D. Schuh, D. Bougeard, H. Ebert, D. Weiss, and C. H. Back, *Nat. Phys.* **14**, 490 (2018).
- [78] D. F. Jackson Kimball, A. O. Sushkov, and D. Budker, *Phys. Rev. Lett.* **116**, 190801 (2016).
- [79] J. Walowski, M. Djordjevic Kaufmann, B. Lenk, C. Hamann, J. McCord, and M. Munzenberg, *J. Phys. D: Appl. Phys.* **41**, 164016 (2008).
- [80] D. M. Lattery, D. Zhang, J. Zhu, X. Hang, J.-P. Wang, and X. Wang, *Sci. Rep.* **8**, 13395 (2018).
- [81] Y. Zhao, Q. Song, S.-H. Yang, T. Su, W. Yuan, S. S. P. Parkin, J. Shi, and Wei Han, *Sci. Rep.* **6**, 22890 (2016).
- [82] I. Barsukov, S. Mankovsky, A. Rubacheva, R. Meckenstock, D. Spoddig, J. Lindner, N. Melnichak, B. Krumme, S. I. Makarov, H. Wende, H. Ebert, and M. Farle, *Phys. Rev. B* **84**, 180405(R) (2011).
- [83] Y. Liu, Z. Yuan, R. J. H. Wesselink, A. A. Starikov, and Paul J. Kelly, *Phys. Rev. Lett.* **113**, 207202 (2014).
- [84] Q. Qin, S. He, W. Song, P. Yang, Q. Wu, Y. P. Feng, and J. Chen, *Appl. Phys. Lett.* **110**, 112401 (2017).
- [85] A. A. Serga, A. V. Chumak, and B. Hillebrands, *J. Phys. D: Appl. Phys.* **43**, 264002 (2010).
- [86] C. Y. You, *Appl. Phys. Express* **5**, 103001 (2012).
- [87] A. I. Liechtenstein, M. I. Katsnelson, V. P. Antropov, and V. A. Gubanov, *J. Magn. Mater.* **67**, 65 (1987).
- [88] M. J. Han, T. Ozaki, and J. Yu, *Phys. Rev. B* **70**, 184421 (2004).

- [89] M. A. Ruderman and C. Kittel, *Phys. Rev.* **96**, 99 (1954); T. Kasuya, *Prog. Theor. Phys.* **16**, 45 (1956); K. Yosida, *Phys. Rev.* **106**, 893 (1957).
- [90] J. B. Goodenough, *Phys. Rev.* **100**, 564 (1955); J. Kanamori, *J. Appl. Phys.* **31**, S14 (1960); P. W. Anderson, *Phys. Rev.* **115**, 2 (1959).
- [91] M. Pajda, J. Kudrnovský, I. Turek, V. Drchal, and P. Bruno, *Phys. Rev. B* **64**, 174402 (2001).
- [92] O. Šipr, S. Mankovsky, and H. Ebert, *Phys. Rev. B* **100**, 024435 (2019).
- [93] A. M. Pradipto, T. Akiyama, T. Ito, and K. Nakamura, *Phys. Rev. B* **96**, 014425 (2017).
- [94] Y. Yin, F. Pan, M. Ahlberg, M. Ranjbar, P. Dürrenfeld, A. Houshang, M. Haidar, L. Bergqvist, Y. Zhai, R. K. Dumas, A. Delin, and J. Akerman, *Phys. Rev. B* **92**, 024427 (2015).
- [95] S. Klingler, A. V. Chumak, T. Mewes, B. Khodadadi, C. Mewes, C. Dubs, O. Surzhenko, B. Hillebrands, and A. Conca, *J. Phys. D: Appl. Phys.* **48**, 015001 (2015).
- [96] J. L. Lado, and J. Fernández-Rossier, *2D Mater.* **4**, 035002 (2017).
- [97] J. M. Dixon, J. A. Tuszynski, and E. J. Carpenter, *Physica A* **349**, 487 (2005).
- [98] X. Li and J. Yang, *J. Mater. Chem. C* **2**, 7071 (2014).